SCIENCE CHINA Materials ARTICLES

mater.scichina.com link.springer.com

Published online 17 June 2021 | https://doi.org/10.1007/s40843-021-1681-7
Sci China Mater 2021, 64(11): 2667–2674

Lead-free rare-earth double perovskite $Cs_2AgIn_{1-y-x}Bi_xLa_yCl_6$ nanocrystals with highly efficient warm-white emission

Hang Yin[1,2], Qingkun Kong[1], Ruiling Zhang[1], Daoyuan Zheng[1], Bin Yang[2] and Keli Han[1,2*]

ABSTRACT **Lead-free double perovskite nanocrystals (NCs), such as $Cs_2AgInCl_6$, have attracted considerable attention as stable and non-toxic alternatives to lead-based perovskites. However, the low photoluminescence (PL) intensity of pristine $Cs_2AgInCl_6$ limits its practical applications. In this study, a series of $Cs_2AgIn_{1-y-x}Bi_xLa_yCl_6$ NCs were synthesized to break the parity-forbidden transition and modify the associated optical functionalities. A broadband bright warm-white emission in the visible region was achieved, with an excellent PL quantum yield of 60%. The dynamic mechanism, involving ultrafast transient absorption, suggests that high-efficiency PL is induced by triplet self-trapping exciton emission. The incorporation of La^{3+}-Bi^{3+} facilitated the singlet–triplet transition by increasing the lifetime and quickening the intersystem crossing process. This finding provides a reliable method for optimizing the optical properties of emerging lead-free halide perovskite NCs.**

Keywords: lead-free, double perovskite, nanocrystal, La^{3+}-Bi^{3+} co-doping, photoluminescence

INTRODUCTION

Lead-free halide perovskite nanocrystals (NCs) have attracted much research attention due to their nontoxicity, finite-size electronic effects, and tunable emission in the visible region [1–5]. One of the most widely studied all-inorganic lead-free halide double perovskites (DPs) is $Cs_2AgInCl_6$, which has a three-dimensional structure similar to lead halide perovskites (LHPs) exhibiting "defect tolerance" [6–8]. Its large fundamental bandgap makes $Cs_2AgInCl_6$ suitable as a matrix for tuning photoluminescence (PL) [9]. However, the parity-forbidden transition in $Cs_2AgInCl_6$ results in extremely low radiative recombination rates, leading to a low PL quantum yield (PLQY) [10]. To solve this problem and improve its efficiency, one practical approach involves partially substituting Ag^+ or In^{3+} with activator ions [11–13]. Alloying activator ions into $Cs_2AgInCl_6$ NC sustains the DP structure, while breaking the dark transition by altering the symmetry of the wavefunction and reducing the electronic dimensionality [14]. Through extensive research, the PLQY of this type of NCs has been increased up to ~36% [15], which is still impracticably low.

In this study, we synthesized a series of $Cs_2AgIn_{1-y-x}Bi_xLa_yCl_6$ NCs. The electron-shell configuration of lanthanum is $5d^1\ 6s^2$, which is different from that of indium. Therefore, alloying La^{3+} into the lattice of $Cs_2AgInCl_6$ produced an allowed transition, accompanied by a broadband, bright, warm-white emission. However, La^{3+} incorporated into $Cs_2AgInCl_6$ would produce defects. To reduce the number of these defects, La^{3+}-Bi^{3+} was coalloyed to modify the lattice, creating a new lower-energy optical absorption channel. Crucially, the optimized sample exhibited a PLQY of 60%, which is the highest reported value for this type of NCs. The dynamic mechanisms of $Cs_2AgIn_{1-y-x}Bi_xLa_yCl_6$ NCs were further studied by combining the results of steady-state absorption and emission, nanosecond transient emission (nsTE), and femtosecond transient absorption (fsTA).

EXPERIMENTAL SECTION

Materials

Cesium acetate (CsOAc, 99.99%, Alfa Aesar), silver acetate (AgOAc, 99.99%, Alfa Aesar), indium acetate ($In(OAc)_3$, 99.99%, Alfa Aesar), lanthanum acetate ($La(OAc)_3$, 99%, Alfa Aesar), bismuth acetate ($Bi(OAc)_3$, 99.99%, Alfa Aesar), benzoyl chloride (BzCl, 99%, Alfa

[1] Institute of Molecular Sciences and Engineering, Shandong University, Qingdao 266237, China
[2] State Key Laboratory of Molecular Reaction Dynamics, Dalian Institute of Chemical Physics, Chinese Academy of Sciences, Dalian 116023, China
* Corresponding author (email: klhan@dicp.ac.cn)

Aesar), 1-octadecene (ODE, 90%, Alfa Aesar), oleylamine (OLA, Aladdin, 80%), oleic acid (OA, 90%, Alfa Aesar), and *n*-hexane (97%, Aladdin) were used as received.

Synthesis

The $Cs_2AgInCl_6$ NC was prepared by a one-pot hot injection method. Briefly, 1 mmol of CsOAc, 0.5 mmol of AgOAc, and 0.5 mmol of $In(OAc)_3$ were dissolved in a mixture of ODE (10 mL), OA (3 mL), and OLA (0.8 mL), and the mixture was degassed at 110°C under vacuum for 2 h. Thereafter, the solution was heated to 125°C in a N_2 atmosphere. Upon reaching this temperature, 0.40 mL of BzCl in 1.13 mL of ODE was swiftly injected. After 2 min, the reaction mixture was cooled to room temperature using an ice-water bath. This crude reaction solution was centrifuged at 10,000 rpm for 10 min. The brown-colored supernatant was decanted, and the precipitate was resuspended in 5 mL of *n*-hexane and fully dissolved by sonication. This solution was then recentrifuged at 6000 rpm for 8 min. The pellet was discarded, and the supernatant was collected and stored under inert conditions.

$Cs_2AgIn_{1-y-x}Bi_xLa_yCl_6$ NCs were synthesized using the same protocol, except adding appropriate amounts of $La(OAc)_3$ or $Bi(OAc)_3$ to the reaction mixture. At $x = 0$, the amounts of $La(OAc)_3$ (fed at $y = 0$, 0.05, 0.15, 0.25, 0.35, and 0.45) were 0, 0.025, 0.075, 0.125, 0.175, and 0.225 mmol, respectively, for $Cs_2AgIn_{1-y}La_yCl_6$ NCs. The optimum value of y was found to be 0.25 (0.125 mmol), for which the best PL properties were obtained. Therefore, we finalized this composition when synthesizing $Cs_2AgIn_{0.75-x}Bi_xLa_{0.25}Cl_6$ NCs. The amounts of $Bi(OAc)_3$ and $In(OAc)_3$ (fed at $x = 0.15$, 0.30, 0.45, 0.60, and 0.75) were 0.075, 0.15, 0.225, 0.30, and 0.375 mmol, and 0.30, 0.225, 0.15, 0.075, and 0.00 mmol, respectively. All the NCs prepared were dispersed in *n*-hexane to form colloidal solutions.

RESULTS AND DISCUSSION

To separately investigate the effect of La^{3+} substitution on the structure and optical properties of the NCs, we initially did not incorporate Bi^{3+} into NCs, i.e., $x = 0$. The powder X-ray diffraction (PXRD) pattern of $Cs_2AgInCl_6$ NCs (Fig. S1) shows that it crystallizes in the *Fm*-3*m* space group of the face-centered cubic crystal system. The PXRD patterns for $Cs_2Ag\ In_{1-y}La_yCl_6$ ($y = 0$, 0.05, 0.15, 0.25, 0.35, 0.45) are shown in Fig. 1a. As the amount of incorporated La^{3+} increased, the (220) peak shifted monotonically towards higher 2θ values, probably because La^{3+} has a larger ionic radius (104 pm) than In^{3+} (94 pm). Such inhomogeneity of ionic radii may alter the crystal symmetry and create lattice defects. This material

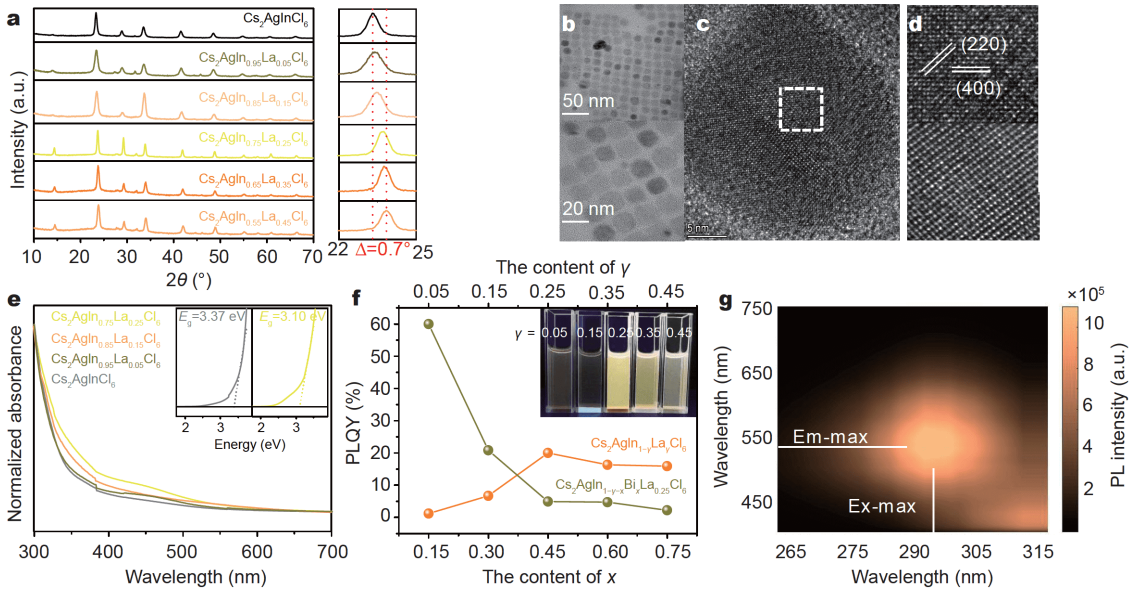

Figure 1 (a) XRD patterns of the NC powders for $Cs_2AgIn_{1-y}La_yCl_6$ ($y = 0$, 0.05, 0.15, 0.25, 0.35, 0.45). (b) TEM and (c) HRTEM images of $Cs_2AgIn_{0.75}La_{0.25}Cl_6$ NC. (d) HRTEM images of $Cs_2AgIn_{0.75}La_{0.25}Cl_6$ (top) and pristine $Cs_2AgInCl_6$ NCs (bottom). (e) Absorption spectra of NCs in hexane solution. The insets are the Tauc plots of the band edge transition for $Cs_2AgIn_{0.75}La_{0.25}Cl_6$ and pristine $Cs_2AgInCl_6$ NCs. (f) PLQY for $Cs_2AgIn_{1-y-x}Bi_xLa_yCl_6$ (while $x = 0$ represents $Cs_2AgIn_{1-y}La_yCl_6$, $y = 0.05$, 0.15, 0.25, 0.35, 0.45; while $y = 0.25$ represents $Cs_2AgIn_{0.75-x}Bi_xLa_{0.25}Cl_6$, $x = 0.15$, 0.30, 0.45, 0.60, 0.75, respectively). (g) EEM spectrum for $Cs_2AgIn_{0.75}La_{0.25}Cl_6$.

exhibited relatively high stability in air, exposure to which did not alter its diffraction peaks even after three months. The defects formed due to the substitution of In^{3+} by La^{3+} were observed in the transmission electron microscopy (TEM). As shown in Fig. 1b and Fig. S2, the $Cs_2AgIn_{0.75}La_{0.25}Cl_6$ NCs were cubical in shape with edge lengths of ~13.3 nm and retained their size distribution and structural integrity. The results of scanning transmission electron microscopy–energy-dispersive X-ray spectroscopy (STEM-EDS) (Fig. S3 and Table S1) are close to those of inductively coupled plasma-optical emission spectrometry (ICP-OES) (Table S2), roughly matching the In/La ratio in the precursor. The high-resolution TEM (HRTEM) images (Fig. 1c and d) confirm the lattice spacing values of 3.70 and 2.63 Å, corresponding to the (220) and (400) planes, respectively.

However, the number of inherent crystal defects found in the $Cs_2AgIn_{1-y}La_yCl_6$ samples (Fig. 1d, top) was larger than that found in pristine $Cs_2AgInCl_6$ NCs (Fig. 1d, bottom). The microstructure of the defects may affect their corresponding optical properties. Their steady-state absorption spectra (Fig. 1e and Fig. S4) showed that the Urbach tail became monotonically stronger and longer with increasing La^{3+} fraction. These features may be attributed to the structural disorder induced by the formation of intrinsic defect [16–18], which agrees well with the aforementioned HRTEM results. The PL excitation (PLE) spectra for $Cs_2AgIn_{0.75}La_{0.25}Cl_6$ obtained at different emission wavelengths are shown in Fig. S5. Relative to its absorption spectrum, another intrinsic PLE peak appeared at 345 nm, corresponding to the absorption band edge range. The peak position did not change upon tuning the monitored wavelength. This result confirmed the existence of defects, which may be crucial for breaking the dark transition. The parity-forbidden transition for $Cs_2AgInCl_6$ NCs occurs at ~300 nm [19], and the modified absorption band edge may alter the associated transition and optical bandgap. The detailed absorption spectra in the vicinity of the absorption onset (1.75–3.75 eV) for $Cs_2AgIn_{0.75}La_{0.25}Cl_6$ and pristine $Cs_2AgInCl_6$ NCs are shown in the inset of Fig. 1e. Compared with the previously reported generally recognized bandgap (3.37 eV) of $Cs_2AgInCl_6$ [20], the significantly decreased absorption onset energy, depicted in the Tauc plot, indicated the narrowing of the bandgap (3.10 eV) due to La^{3+} alloying.

According to previously published reports, defect formation is highly likely to result in unpredictable PL [21,22]. As expected, significant differences in intensity were observed between the PL spectra of pristine $Cs_2AgInCl_6$ and $Cs_2AgIn_{0.75}La_{0.25}Cl_6$, following excitation at 295 nm (Fig. S6). The PL intensity of $Cs_2AgInCl_6$ was found to be very low, with the PLQY being <1%, while a broadband bright warm-white emission was achieved for a La^{3+} fraction of 25%, with the PLQY being ~20% (Fig. S7). At this excitation wavelength, $Cs_2AgIn_{0.75}La_{0.25}Cl_6$ exhibited an emission intensity ~60 times higher than that for $Cs_2AgIn_{0.95}La_{0.05}Cl_6$. With further increase in La^{3+} fraction, the bright PL emission dimmed gradually (Fig. 1f), and the PL peaks exhibited a gradual hypsochromic shift (Fig. S8). Even more detrimentally, the NCs became unstable and difficult to synthesize at La^{3+} fractions >25%. Hence, we consider $y = 0.25$ to be the optimum La^{3+} fraction. The overall PL emission for $Cs_2AgIn_{0.75}La_{0.25}Cl_6$ can be estimated from the total luminescence spectra (excitation-emission-matrix spectra, EEMs), as shown in Fig. 1g. The strongest PL peak originated from the maximum excitation at 293 nm, which may be inferred to be a parity-allowed transition.

The incorporation of Bi^{3+} is believed to improve crystal perfection and promote exciton localization [23,24]. Therefore, La^{3+}-Bi^{3+} coalloying may be a feasible approach to modify the lattice structure further in order to tune the optical properties. For maintaining the aforementioned optimum La^{3+} fraction, a series of $Cs_2AgIn_{0.75-x}Bi_xLa_{0.25}Cl_6$ NCs were synthesized for x = 0.15, 0.30, 0.45, 0.60, and 0.75. The XRD patterns of all the $Cs_2AgIn_{0.75-x}Bi_xLa_{0.25}Cl_6$ NCs are depicted in Fig. 2a and Fig. S9. The peaks corresponding to the (022) plane (Fig. S10) showed a monotonic shift to smaller diffraction angles with increasing Bi^{3+} fraction due to the lattice contraction, consistent with previously reported results for Bi^{3+}-alloyed $Cs_2AgInCl_6$ [15]. The successful alloying of Bi^{3+} ions was confirmed by the results of X-ray photoelectron spectroscopy (XPS) (Fig. S11). The detailed TEM images are shown in Fig. S12. As expected, the HRTEM image of $Cs_2AgIn_{0.6}Bi_{0.15}La_{0.25}Cl_6$ NC (Fig. 2b) revealed high crystallinity. The STEM-EDS elemental-mapping images for each element in $Cs_2AgIn_{0.6}Bi_{0.15}La_{0.25}Cl_6$ (Fig. 2c) attested to the homogeneous elemental distribution colocalized in NCs. With increasing Bi^{3+} fraction, the NCs exhibited distinct modification to their optical properties.

The suppressed absorption tail of $Cs_2AgIn_{0.75-x}Bi_xLa_{0.25}Cl_6$ confirmed the effective tuning of sub-bandgap defect states. With increasing Bi^{3+} fraction, the excitonic peak exhibited a slight red shift, particularly in $Cs_2AgIn_{0.6}Bi_{0.15}La_{0.25}Cl_6$. An intense excitonic peak at ~380 nm was observed (Fig. 2d), which might arise from the direct Bi^{3+} s-p transition [25,26]. At this excitation wavelength,

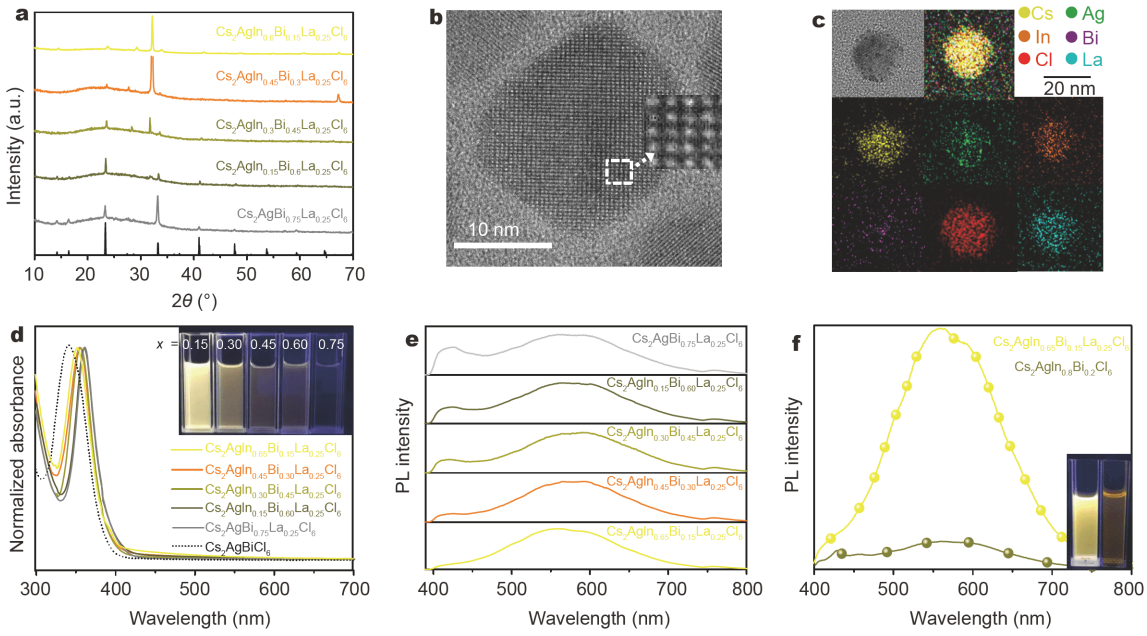

Figure 2 (a) XRD patterns of the NC powders for $Cs_2AgIn_{0.75-x}Bi_xLa_{0.25}Cl_6$ ($0.15 \leq x \leq 0.75$) and reported XRD pattern for $Cs_2AgBiCl_6$ (ICSD 291598). (b) HRTEM image of $Cs_2AgIn_{0.6}Bi_{0.15}La_{0.25}Cl_6$ NC. (c) Elemental mappings in $Cs_2AgIn_{0.6}Bi_{0.15}La_{0.25}Cl_6$ NC. (d) NC absorption spectra in hexane solutions. The inset is the image of $Cs_2AgIn_{0.75-x}Bi_xLa_{0.25}Cl_6$ NCs under 365-nm UV light. (e) Normalized PL spectra for $Cs_2AgIn_{0.75-x}Bi_xLa_{0.25}Cl_6$ NCs. (f) PL spectra of $Cs_2AgIn_{0.6}Bi_{0.15}La_{0.25}Cl_6$ and $Cs_2AgIn_{0.8}Bi_{0.2}Cl_6$ NCs. The inset is the image of $Cs_2AgIn_{0.6}Bi_{0.15}La_{0.25}Cl_6$ (left) and $Cs_2AgIn_{0.8}Bi_{0.2}Cl_6$ (right) NCs under 365-nm UV light.

$Cs_2AgIn_{0.75-x}Bi_xLa_{0.25}Cl_6$ NCs exhibited a broadband emission with a peak at ~560 nm (Fig. 2e). In addition, the weak PL peak at 395 nm corresponds to the band-edge exciton emission, as demonstrated in our previous study [27]. The strong PL peak at ~560 nm exhibited a slight red shift as x increased from 0.15 to 0.75. Under this condition, the color temperatures increased monotonically based on the locus of points in a chromaticity coordinate diagram (Fig. S13). Increasing the Bi^{3+} fraction gradually decreased the PLQYs (Fig. 1f) and PL intensities (Fig. S14) of $Cs_2AgIn_{0.75-x}Bi_xLa_{0.25}Cl_6$ NCs. Particularly, $Cs_2AgIn_{0.6}Bi_{0.15}La_{0.25}Cl_6$ showed an emission intensity ~50 times higher than that of $Cs_2AgIn_{0.8}Bi_{0.2}Cl_6$ at an identical In^{3+}/Bi^{3+} ratio (Fig. 2f), indicating that La^{3+}-Bi^{3+} coalloying is an effective approach to further enhancing the efficiencies of NCs. The PLQY was increased by 60%, which is the highest value reported thus far (Fig. S7). Interestingly, the PL spectrum of $Cs_2AgIn_{0.6}Bi_{0.15}La_{0.25}Cl_6$ strongly resembles that of $Cs_2AgIn_{0.75}La_{0.25}Cl_6$, and large Stokes shifts are evident in both cases. This indicates that the effective radiative transition may originate from the same energy state due to similar charge-carrier trapping processes.

To evaluate the intrinsic nature of the charge-carrier trapping process, we carried out PL measurements over the temperature range of 80–300 K. Fig. 3a, b show the pseudo-color plots for $Cs_2AgIn_{0.75}La_{0.25}Cl_6$ and $Cs_2AgIn_{0.6}Bi_{0.15}La_{0.25}Cl_6$, respectively. Both compounds exhibited higher PL intensities at lower temperatures. Interestingly, an additional PL peak at ~480 nm was observed at lower temperatures (Fig. 3a), indicating that $Cs_2AgIn_{0.75}La_{0.25}Cl_6$ exhibits dual radiative recombination. Fig. 3c and Fig. S15a show that the PL intensity of $Cs_2AgIn_{0.75}La_{0.25}Cl_6$ did not change appreciably over the entire tested temperature range, with the maximum intensity being exhibited at 250 K. The temperature-stable emission suggests that the outermost electron of La^{3+} is effectively screened from the surrounding defect sites by the closed $5s^25p^6$ outer shell of La^{3+}. In contrast, the emission of $Cs_2AgIn_{0.6}Bi_{0.15}La_{0.25}Cl_6$ is evidently dependent on temperature, with its PL intensity increasing with decreasing temperature. The intensity curve plateaus at temperatures below 200 K, which arise from a thermally driven back being more difficult at lower temperatures [28]. The exciton-phonon coupling strength also plays an important role in the charge-carrier trapping process [29,30]. Fig. 3d summarizes and compares the PL full width at half maximum (FWHM) of the two materials. The significant change in the PL FWHM with temperature can be attributed to the strong exciton-phonon

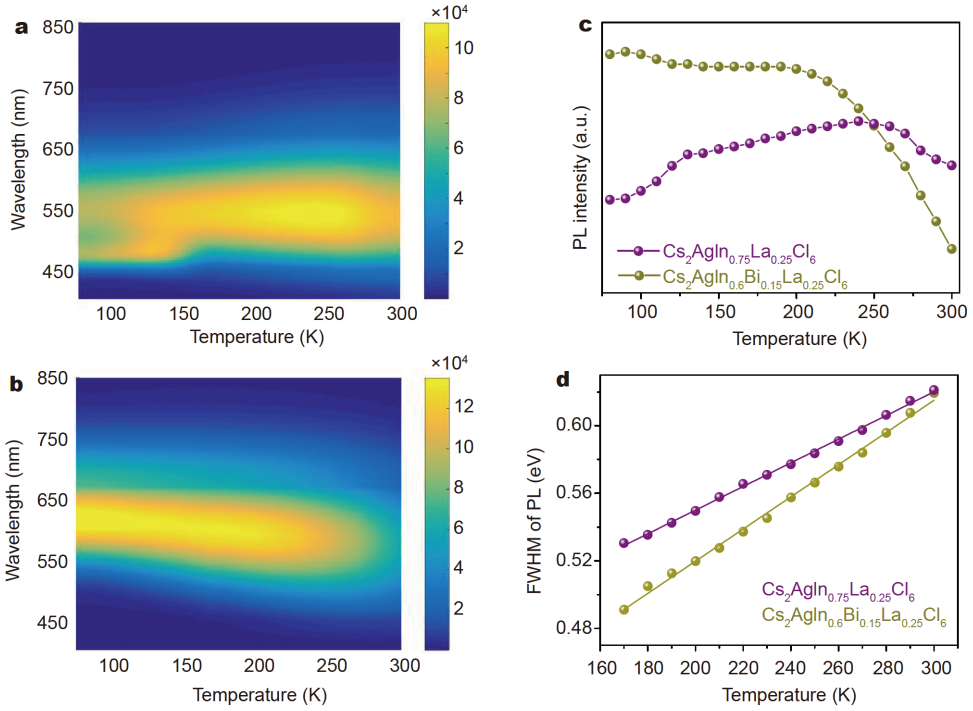

Figure 3 Pseudo-color plots of temperature-dependent PL spectra from 80 to 300 K of (a) $Cs_2AgIn_{0.75}La_{0.25}Cl_6$ and (b) $Cs_2AgIn_{0.6}Bi_{0.15}La_{0.25}Cl_6$. (c) Temperature-dependent PL peak intensities and (d) FWHMs of $Cs_2AgIn_{0.75}La_{0.25}Cl_6$ and $Cs_2AgIn_{0.6}Bi_{0.15}La_{0.25}Cl_6$.

coupling [31]. In this study, the FWHMs of $Cs_2AgIn_{0.75}La_{0.25}Cl_6$ and $Cs_2AgIn_{0.6}Bi_{0.15}La_{0.25}Cl_6$ broaden from 540 and 480 meV to 621 and 660 meV, respectively. Both the longitudinal optical (LO) phonon modes are located at ~295 cm^{-1} ($E_{LO} \approx 36$ meV), as determined from the Raman spectrum measurements (Fig. S16). Based on these parameters, the fitted electron-coupling constant for the former is $\gamma_{LO} = 210$ meV and that for the latter is $\gamma_{LO} = 330$ meV. The strong carrier-phonon coupling may induce intrinsic self-traps.

The linear dependence of the PL intensity at 560 nm on the excitation power density (0.37–51.4 mW) (Fig. S17) suggests that the emission does not arise from permanent defects. A probable reason for the large Stokes shift, strong carrier-phonon coupling, and broad emission is the self-trapping exciton (STE)-emission, as observed in other DPs [32,33]. Since band edge states do not influence STEs [34], $Cs_2AgIn_{0.75-x}Bi_xLa_{0.25}Cl_6$ NCs may reasonably change their bandgaps, without affecting the position of their PL peaks. To unveil the entire dynamics of the decay process, we then performed nsTE spectroscopy. Fig. 4a reveals a microsecond-long lifetime across the visible region, which may be justifiably assigned as the triplet STE-emission. La^{3+} incorporation dramatically prolongs the PL lifetimes by dozens of orders of magnitude (Fig. S18). The long-lived component of the $Cs_2AgIn_{0.6}Bi_{0.15}La_{0.25}Cl_6$ NC (~7.2 μs) is longer than that of the $Cs_2AgIn_{0.75}La_{0.25}Cl_6$ NC (~3.0 μs), as shown in Fig. 4b. These values are consistent with the results obtained from the time-resolved PL (TRPL) measurements using time-correlated single-photon counting (TCSPC) (Fig. 4c and Fig. S19). With increasing Bi^{3+} content in $Cs_2AgIn_{0.75-x}Bi_xLa_{0.25}Cl_6$ NCs, the lifetimes changed significantly when probed at 560 nm. Compared with the other studied Bi^{3+} contents in $Cs_2AgIn_{0.75-x}Bi_xLa_{0.25}Cl_6$ NCs, the $Cs_2AgIn_{0.6}Bi_{0.15}La_{0.25}Cl_6$ NC exhibited slower decay at 560 nm. Generally, the trend of longer PL lifetimes was accompanied by enhanced PLQYs, illustrating that adding reasonable Bi^{3+} contents could be an effective approach to inhibiting the non-radiative recombination processes. The TCSPC was measured at low temperatures (Fig. S20) to investigate the difference between $Cs_2AgIn_{0.75}La_{0.25}Cl_6$ and $Cs_2AgIn_{0.6}Bi_{0.15}La_{0.25}Cl_6$. At 80 K, the component at ~800 ns dominates the radiative recombination (99.99%) in $Cs_2AgIn_{0.75}La_{0.25}Cl_6$ NC, suggesting that intersystem crossing (ISC) was thermally inhibited at low temperatures. In this case, the PL emission at 480 nm may be retained for singlet STE-emission. In contrast, there are few changed lifetimes in $Cs_2AgIn_{0.6}Bi_{0.15}La_{0.25}Cl_6$ NC at low temperatures (Fig. S20b).

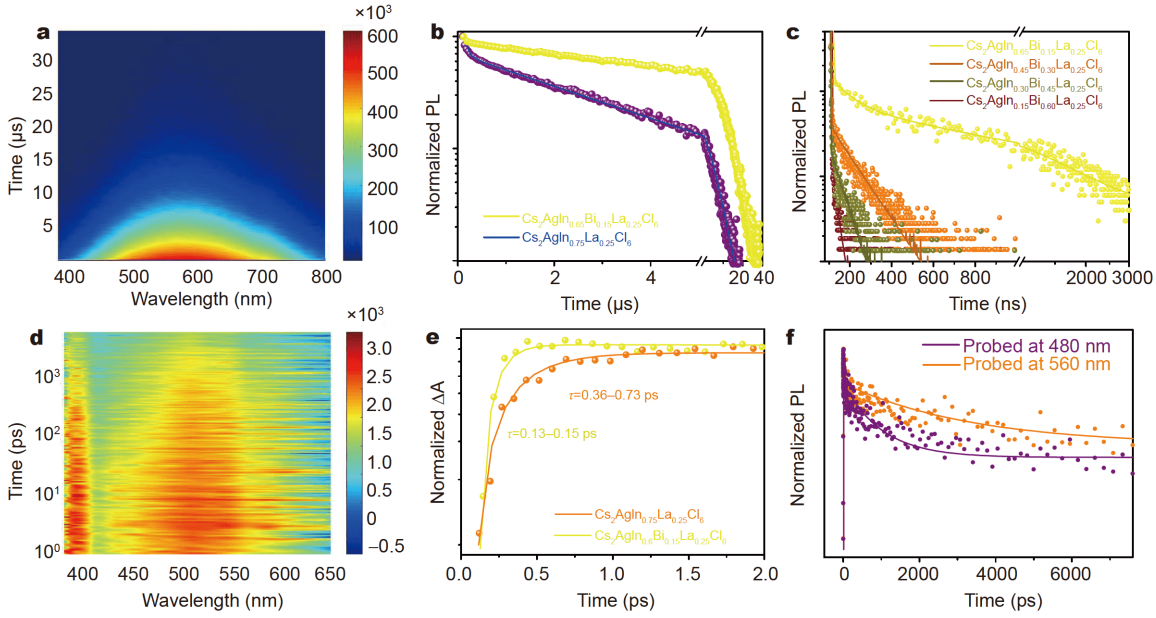

Figure 4 (a) Pseudo-color plot of nsTE spectroscopic analysis of the $Cs_2AgIn_{0.6}Bi_{0.15}La_{0.25}Cl_6$ NC. (b) TE spectra probed at 560 nm. (c) TRPL kinetics of $Cs_2AgIn_{0.75-x}Bi_xLa_{0.25}Cl_6$ NCs. (d) Pseudo-color TA plot of $Cs_2AgIn_{0.75}La_{0.25}Cl_6$ NC. (e) Normalized PIA onsets for $Cs_2AgIn_{0.75}La_{0.25}Cl_6$ and $Cs_2AgIn_{0.6}Bi_{0.15}La_{0.25}Cl_6$. (f) TA kinetics of $Cs_2AgIn_{0.75}La_{0.25}Cl_6$ probed at 480 and 560 nm.

To investigate the photophysical process in detail, we performed fsTA (pump-probe) spectroscopy, which could provide more direct evidence for exciton self-trapping. The pseudo-color TA plots for $Cs_2AgIn_{0.75}La_{0.25}Cl_6$ and $Cs_2AgIn_{0.6}Bi_{0.15}La_{0.25}Cl_6$ NCs, as functions of wavelength and decay time, are presented in Fig. 4d and Fig. S21, respectively. Both are observed under a broadband photo-induced absorption (PIA) signal (Fig. S22) near the steady-state emission range, which may be considered direct evidence for the formation of STEs [28,35]. The rise times of the PIA bands are plotted in Fig. 4e and Fig. S23 to evaluate the formation of STEs. Fig. 4e shows that the formation process of $Cs_2AgIn_{0.75}La_{0.25}Cl_6$ is considerably slower (0.36–0.73 ps) than that of $Cs_2AgIn_{0.6}Bi_{0.15}La_{0.25}Cl_6$ (0.13–0.15 ps), indicating that the narrower potential barrier induced carrier transport upon La^{3+}-Bi^{3+} coalloying. The faster formation process may be attributed to the lowered excitation energy of Bi^{3+}. For the $Cs_2AgIn_{0.75}La_{0.25}Cl_6$ NC probed at 560 nm, the PIA decay signal (Fig. 4f) can be fitted by three time scales: an ultrashort lifetime of 0.25–0.33 ps, a middling lifetime of ~40 ps, and a prolonged lifetime of >8 ns. As mentioned earlier, the long-lived component has been observed by nsTE spectroscopy, and is attributed to the triplet STE-emission. However, when probed at 480 nm, the different lifetimes for the long-lived component confirmed that dual STEs coexist in the radiative transition process of the $Cs_2AgIn_{0.75}La_{0.25}Cl_6$ NC. Therefore, it follows that the PIA decay curve of the $Cs_2AgIn_{0.6}Bi_{0.15}La_{0.25}Cl_6$ NC would not possess the component of ~40 ps, which is only fitted by an ultrashort lifetime of 0.35–0.43 ps and a prolonged lifetime of >8 ns. The absent middling lifetime is reasonable evidence for the trapping of inherent crystal defects, consistent with the results of our previous study [36]. In addition, the ultrashort component exists in both materials and may be attributed to the ISC process from the singlet to the triplet exciton state. The higher ISC rate raises the singlet exciton fully to triplet STE states, proving the effectiveness of defect engineering by incorporating Bi^{3+} to promote localization of triplet excitons. The broken symmetry-forbidden transition for $Cs_2AgIn_{0.6}Bi_{0.15}La_{0.25}Cl_6$ would result in high-efficiency triplet STE-emission. Consequently, the radiative transition eventually presents a bright warm-white emission. The hypothetical photophysical process models are depicted in Fig. S24.

CONCLUSIONS

In summary, we have successfully synthesized a series of $Cs_2AgIn_{1-y-x}Bi_xLa_yCl_6$ NCs. Herein, we propose that alloying lanthanum or bismuth ions into colloidal $Cs_2AgInCl_6$ NCs can break the parity-forbidden transition and modify their optical functionalities. Among all the compounds investigated in this study, $Cs_2AgIn_{0.6}$-

$Bi_{0.15}La_{0.25}Cl_6$ exhibited the best PL properties, with a broadband bright warm-white emission. To the best of our knowledge, this is the highest PLQY obtained for this class of materials. The dynamic PL mechanisms for $Cs_2AgIn_{0.75}La_{0.25}Cl_6$ and $Cs_2AgIn_{0.6}Bi_{0.15}La_{0.25}Cl_6$ suggest that high-efficiency PL resulted from triplet STE-emission. La^{3+}-Bi^{3+} incorporation improved the lattice defects, created new optical absorption channels, and lowered the potential barrier, thereby facilitating the transition of the singlet exciton fully to triplet STE states, increasing the PL lifetime, and expediting the ISC process. These factors contribute significantly to the enhancement of the PL. We hope that this strategy will help tune the optical functionalities of other DPs in the future.

Received 5 February 2021; accepted 30 March 2021; published online 17 June 2021

1 Fan Q, Biesold-McGee GV, Ma J, *et al.* Lead-free halide perovskite nanocrystals: Crystal structures, synthesis, stabilities, and optical properties. Angew Chem Int Ed, 2020, 59: 1030–1046
2 Yang B, Han K. Charge-carrier dynamics of lead-free halide perovskite nanocrystals. Acc Chem Res, 2019, 52: 3188–3198
3 Jellicoe TC, Richter JM, Glass HFJ, *et al.* Synthesis and optical properties of lead-free cesium tin halide perovskite nanocrystals. J Am Chem Soc, 2016, 138: 2941–2944
4 Pal J, Manna S, Mondal A, *et al.* Colloidal synthesis and photophysics of $M_3Sb_2I_9$ (M=Cs and Rb) nanocrystals: Lead-free perovskites. Angew Chem Int Ed, 2017, 56: 14187–14191
5 Xiao Z, Song Z, Yan Y. From lead halide perovskites to lead-free metal halide perovskites and perovskite derivatives. Adv Mater, 2019, 31: 1803792
6 Guo ZY, Li CX, Gao M, *et al.* Mn−O covalency governs the intrinsic activity of Co-Mn spinel oxides for boosted peroxymonosulfate activation. Angew Chem Int Ed, 2021, 60: 274–280
7 Volonakis G, Haghighirad AA, Milot RL, *et al.* $Cs_2InAgCl_6$: A new lead-free halide double perovskite with direct band gap. J Phys Chem Lett, 2017, 8: 772–778
8 Brandt RE, Stevanović V, Ginley DS, *et al.* Identifying defect-tolerant semiconductors with high minority-carrier lifetimes: Beyond hybrid lead halide perovskites. MRS Commun, 2015, 5: 265–275
9 Manna D, Das TK, Yella A. Tunable and stable white light emission in Bi^{3+}-alloyed $Cs_2AgInCl_6$ double perovskite nanocrystals. Chem Mater, 2019, 31: 10063–10070
10 Meng W, Wang X, Xiao Z, *et al.* Parity-forbidden transitions and their impact on the optical absorption properties of lead-free metal halide perovskites and double perovskites. J Phys Chem Lett, 2017, 8: 2999–3007
11 Hu Q, Niu G, Zheng Z, *et al.* Tunable color temperatures and efficient white emission from $Cs_2Ag_{1-x}Na_xIn_{1-y}Bi_yCl_6$ double perovskite nanocrystals. Small, 2019, 15: 1903496
12 Liu Y, Jing Y, Zhao J, *et al.* Design optimization of lead-free perovskite $Cs_2AgInCl_6$:Bi nanocrystals with 11.4% photoluminescence quantum yield. Chem Mater, 2019, 31: 3333–3339
13 Liu Y, Rong X, Li M, *et al.* Incorporating rare-earth terbium(III) ions into $Cs_2AgInCl_6$:Bi nanocrystals toward tunable photoluminescence. Angew Chem Int Ed, 2020, 59: 11634–11640
14 Zhu D, Zito J, Pinchetti V, *et al.* Compositional tuning of carrier dynamics in $Cs_2Na_{1-x}Ag_xBiCl_6$ double-perovskite nanocrystals. ACS Energy Lett, 2020, 5: 1840–1847
15 Yang B, Mao X, Hong F, *et al.* Lead-free direct band gap double-perovskite nanocrystals with bright dual-color emission. J Am Chem Soc, 2018, 140: 17001–17006
16 Wang L, Liu H, Zhang Y, *et al.* Photoluminescence origin of zero-dimensional Cs_4PbBr_6 perovskite. ACS Energy Lett, 2020, 5: 87–99
17 Rincón C, Wasim SM, Márquez R, *et al.* Optical properties of the ordered defect compound $CuIn_5Te_8$. J Phys Chem Solids, 2002, 63: 581–589
18 Zhou L, Liao JF, Huang ZG, *et al.* Intrinsic self-trapped emission in 0D lead-free $(C_4H_{14}N_2)_2In_2Br_{10}$ single crystal. Angew Chem, 2019, 131: 15581–15586
19 Lee W, Hong S, Kim S. Colloidal synthesis of lead-free silver–indium double-perovskite $Cs_2AgInCl_6$ nanocrystals and their doping with lanthanide ions. J Phys Chem C, 2019, 123: 2665–2672
20 Zhou J, Xia Z, Molokeev MS, *et al.* Composition design, optical gap and stability investigations of lead-free halide double perovskite $Cs_2AgInCl_6$. J Mater Chem A, 2017, 5: 15031–15037
21 Seth S, Samanta A. Photoluminescence of zero-dimensional perovskites and perovskite-related materials. J Phys Chem Lett, 2018, 9: 176–183
22 Milstein TJ, Kroupa DM, Gamelin DR. Picosecond quantum cutting generates photoluminescence quantum yields over 100% in ytterbium-doped $CsPbCl_3$ nanocrystals. Nano Lett, 2018, 18: 3792–3799
23 Moser F, Lyu S. Luminescence in pure and I-doped AgBr crystals. J Lumin, 1971, 3: 447–458
24 Zhou J, Rong X, Zhang P, *et al.* Manipulation of Bi^{3+}/In^{3+} transmutation and Mn^{2+}-doping effect on the structure and optical properties of double perovskite $Cs_2NaBi_{1-x}In_xCl_6$. Adv Opt Mater, 2019, 7: 1801435
25 Bekenstein Y, Dahl JC, Huang J, *et al.* The making and breaking of lead-free double perovskite nanocrystals of cesium silver–bismuth halide compositions. Nano Lett, 2018, 18: 3502–3508
26 Tan Z, Li J, Zhang C, *et al.* Highly efficient blue-emitting Bi-doped Cs_2SnCl_6 perovskite variant: Photoluminescence induced by impurity doping. Adv Funct Mater, 2018, 28: 1801131
27 Cong M, Yang B, Hong F, *et al.* Self-trapped exciton engineering for white-light emission in colloidal lead-free double perovskite nanocrystals. Sci Bull, 2020, 65: 1078–1084
28 Hu T, Smith MD, Dohner ER, *et al.* Mechanism for broadband white-light emission from two-dimensional (110) hybrid perovskites. J Phys Chem Lett, 2016, 7: 2258–2263
29 McCall KM, Stoumpos CC, Kostina SS, *et al.* Strong electron–phonon coupling and self-trapped excitons in the defect halide perovskites $A_3M_2I_9$ (A = Cs, Rb; M = Bi, Sb). Chem Mater, 2017, 29: 4129–4145
30 Steele JA, Puech P, Keshavarz M, *et al.* Giant electron–phonon coupling and deep conduction band resonance in metal halide double perovskite. ACS Nano, 2018, 12: 8081–8090
31 Ghosh S, Shi Q, Pradhan B, *et al.* Phonon coupling with excitons and free carriers in formamidinium lead bromide perovskite nanocrystals. J Phys Chem Lett, 2018, 9: 4245–4250
32 Zhang R, Mao X, Yang Y, *et al.* Air-stable, lead-free zero-dimensional mixed bismuth-antimony perovskite single crystals with ultra-broadband emission. Angew Chem Int Ed, 2019, 58: 2725–2729
33 Yang B, Hong F, Chen J, *et al.* Colloidal synthesis and charge-

carrier dynamics of $Cs_2AgSb_{1-y}Bi_yX_6$ (X: Br, Cl; $0 \le y \le 1$) double perovskite nanocrystals. Angew Chem Int Ed, 2019, 58: 2278–2283
34 Li S, Luo J, Liu J, *et al.* Self-trapped excitons in all-inorganic halide perovskites: Fundamentals, status, and potential applications. J Phys Chem Lett, 2019, 10: 1999–2007
35 Smith MD, Karunadasa HI. White-light emission from layered halide perovskites. Acc Chem Res, 2018, 51: 619–627
36 Han P, Mao X, Yang S, *et al.* Lead-free sodium–indium double perovskite nanocrystals through doping silver cations for bright yellow emission. Angew Chem Int Ed, 2019, 58: 17231–17235

Acknowledgements This work was financially supported by the National Key Research and Development Program of China (2017YFA0204800), the National Natural Science Foundation of China (21833009, 21533010, and 21525315), the Scientific Instrument Developing Project of the Chinese Academy of Sciences (YJKYYQ20190003), Liaoning Revitalization Talents Program (XLYC1802126), and Dalian City Foundation for Science and Technology Innovation (2019J12GX031).

Author contributions Yin H and Han K conceived the initial idea. Yin H, Kong Q, Zhang R, Zheng D, and Yang B performed the material characterization and analysis. Han K directed the project. All authors discussed the results and commented on the manuscript.

Conflict of interest The authors declare that they have no conflict of interest.

Supplementary information Experimental procedures and supporting data are available in the online version of the paper.

Hang Yin received his Master's degree in physical chemistry from Yanbian University in 2017. He studies at the Institute of Molecular Science and Engineering of Shandong University, instructed by Professor Keli Han from Dalian Institute of Chemical Physics (DICP), Chinese Academy of Sciences (CAS). He is currently jointly trained in Group 1101 of the Key Laboratory of Molecular Dynamics of DICP. He is interested in the research of new energy materials.

Keli Han received his PhD degree in 1990 from the State Key Laboratory of Molecular Reaction Dynamics at DICP and subsequently became an Assistant Professor. He conducted postdoctoral research at the University of California at Davis and Emory University in 1993–1995. In 1995, he became a Full Professor of chemical physics at DICP. His current research interests involve experimental and theoretical chemical dynamics.

具有高效暖白光的非铅稀土双钙钛矿 $Cs_2AgIn_{1-y-x}Bi_xLa_yCl_6$纳米晶

尹航[1,2], 孔庆坤[1], 张瑞玲[1], 郑道元[1], 杨斌[2], 韩克利[1,2*]

摘要 非铅双钙钛矿纳米晶(NCs), 例如$Cs_2AgInCl_6$, 作为稳定、无毒的铅基钙钛矿替代物, 已经引起了人们的广泛关注. 但其较弱的荧光限制了其在实际中的应用. 在这项工作中, 为了打破禁阻跃迁, 同时优化光学特性, 我们合成了一系列$Cs_2AgIn_{1-y-x}Bi_xLa_yCl_6$ NCs. 该材料在可见光区内实现了明亮的宽频带暖白色发光, 量子效率最高达到了60%. 我们利用超快瞬态吸收光谱等先进表征手段研究了其发光动力学机理, 认为高效的白光发射源于三重态自陷激子. La^{3+}和Bi^{3+}的引入延长了荧光衰减寿命并加快了系间窜越进程, 从而促进了单重态–三重态的转换. 这一发现为新型非铅钙钛矿纳米晶材料的光学性能优化提供了可靠的方法.

